

Electrical Transport Properties of Polycrystalline and Amorphous TiO₂ Single Nanotubes

Markus Stiller,^{1,*} Jose Barzola-Quiquia,¹ Pablo Esquinazi,¹ Seulgi So,²
Imgon Hwang,² Patrik Schmuki,² Julia Böttner,³ and Irina Estrela-Lopis³

¹*Division of Superconductivity and Magnetism, Institute for
Experimental Physics II, University of Leipzig, 04103 Leipzig, Germany*

²*Chair for Surface Science and Corrosion Department Material Science and Engineering,
University of Erlangen, D-91058 Erlangen, Germany*

³*Institute of Medical Physics and Biophysics, University of Leipzig, 04107 Leipzig, Germany*
(Dated: February 27, 2017)

The electrical transport properties of anodically grown TiO₂ nanotubes was investigated. Amorphous nanotubes were anodically grown on titanium foil and transformed through annealing into the anatase phase. Amorphous and polycrystalline single nanotubes were isolated and contacted for measurements of the electrical resistance. Non-linear current-voltage characteristics were explained using the fluctuation induced tunneling conduction model. A clear enhancement of the conductance was induced in an insulating anatase nanotube through low-energy Ar/H ion irradiation. Confocal Raman spectroscopy shows that the annealed samples were in anatase phase and a blueshift due to phonon confinement was observed.

PACS numbers: 73.63.Fg, 78.30.Fs

I. INTRODUCTION

Titanium dioxide nanotube arrays, formed by self-organizing anodization, have attracted considerable attention. These 1D structures are used in wide range of applications such as electrodes in catalysis¹, photocatalysis², dye-synthesized solar cells³, gas sensors⁴, photoelectrochemical water splitting^{5,6}, in batteries⁷ or for CO₂ reduction^{8,9}. Biocompatible Ti₄₆Si₁₂O₄₂ nanostructured surfaces can be used to enhance cell attachment and proliferation¹⁰. This outstanding flexibility is a consequence of different electronic, chemical and ionic properties of anatase, brookite and rutile^{11,12}. Anatase is often more interesting for applications, such as solar cells, due to the larger electron mobility compared to rutile.¹³ The combination with the large active surface area of nanostructures, results in a variety of dielectric, conducting, magnetic, catalytic and other physical and chemical properties. Doping can be used to enhance the photo catalytic activity of TiO₂ nanotubes, e.g. with W^{14–16}, Au/W¹⁷, Co^{18,19}, or Co¹⁵.

The general mechanism of electron transport, particularly in nanostructures of TiO₂, is not well studied and understood. Most of the published work focuses on macroscopic samples such as nanotubular arrays^{20,21}, where parasite effects such as contact contributions in two-point (2P) measurements or the scattering of light inside the tangle of tubes, can have considerable influence on the measurements. Depending on the contacts, non-metallic clusters (Au), Schottky barriers (Pt) or oxide layers (Al, Cr) could be formed¹¹. The magnetic^{22,23} and electrical transport properties of TiO₂ depend strongly on structural defects (single crystal band gap: 3.0 – 3.2 eV^{24,25}), such as oxygen or titanium vacancies. The transport properties can also be strongly

influenced by the scattering on the sample surface, as was found for polycrystalline macroscopic arrays of TiO₂ nanotubes²⁶. In addition, it was shown that, intragrain and intergrain conduction processes play an important role in disordered nanowires and nanotubes^{27,28}. Therefore, a large number of different resistivities have been reported, e.g. 10⁴ Ωcm (2P, top/bottom tube contacts)²⁹, 10²...10³ Ωcm³⁰ and 1 Ωcm³¹ using a four-point (4P) probes method. For comparison, the obtained resistivity of different polycrystalline bulk anatase covers a large range: 10²...10⁷ Ωcm^{13,32,33}.

Recently, fluctuation induced tunneling conductance (FITC)³⁴ has been proposed as a responsible mechanism in ZnO nanowires²⁷, in bundles of double-walled carbon nanotubes³⁵ and in nanoporous TiO₂ thin films³⁶. The FITC model predicts non-linear current-voltage $I - V$ curves due to intrinsic barriers between grains in the sample³⁴. Other frequently used mechanisms include variable-range hopping and thermally activated processes. However, they cannot explain the non-linear behavior of $I - V$ curves²⁷ and the saturation of the resistivity at low temperature^{37,38}.

In this work, procedures to isolate single TiO₂ nanotubes and to establish barrier free contacts for electrical transport measurements are presented. The resistance of amorphous and polycrystalline anatase samples were investigated in a broad temperature range. A FITC mechanism contributes to the conductivity in all measured samples with non-linear $I - V$ curves. Additionally, the electrical transport of a highly insulating anatase nanotube was modified by means of defect production at the surface using low-energy ion irradiation.

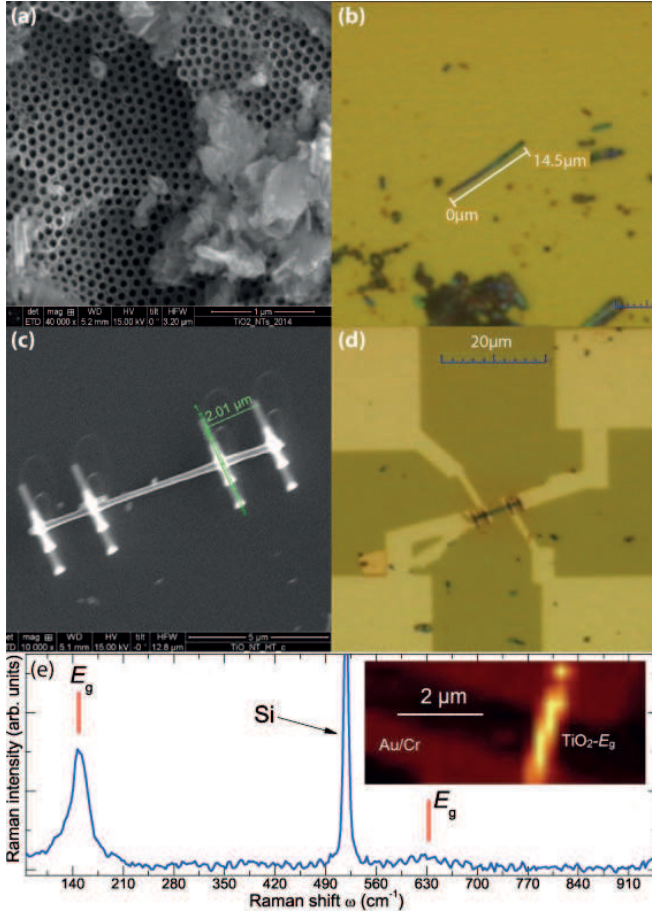


FIG. 1. In (a) a TiO_2 nanotubular array grown on Ti foil is shown. The nanotubes have an average diameter of approximately 120 nm. Figure (b) displays a single TiO_2 nanotube, in (c) the nanotube after WC_x deposition and in (d) the contacted TiO_2 nanotube ready for measurement can be seen. In (e) a Raman image of the investigated sample is shown, the bright region corresponds to the Raman E_g band at 148 cm^{-1} .

II. EXPERIMENTAL

The TiO_2 nanotubes have been separated from nanotubular layers anodically grown on titanium foil (Advent Research Materials Ltd., 99.6 % purity) in an electrochemical cell with ethylene glycol electrolyte containing 0.15 M ammonium fluoride and 1 M H_2O . The titanium foil was anodized with a potential of 60 V applied for 5 hours. Finally, the nanotubular array was placed in ethanol and dried with nitrogen gas. The grown nanotubes (see FIG. 1(a)) are initially in the amorphous phase and were annealed in air using a Rapid Thermal Annealer (Jet-first Rapid Thermal Annealer, Jipilec, France) in order to obtain polycrystalline anatase samples. The heating/cooling rate was $15^\circ\text{C}/\text{min}$ with annealing temperatures of 350°C and 450°C . After annealing, the nanotubes were polycrystalline and exhibited anatase morphology, for more detailed information please refer to Refs.^{39–41}. Annealing at higher tempera-

TABLE I. Overview of the TiO_2 nanotubes presented in this work. The dimensions were measured using scanning electron microscopy. In order to calculate the resistivity of sample NT4 after irradiation, a shell thickness of $d = 5 \text{ nm}$ was assumed.

ID	Phase	Contacts	Length (μm)	$\rho(T = 300\text{K})(\Omega\text{cm})$
NT1	Anatase	4	0.5 ± 0.1	0.026
NT2	Anatase	4	1.5 ± 0.1	0.044
NT3	Amorph	2	3.3 ± 0.2	5.31
NT4	Anatase	2	6.9 ± 0.2	34

tures results in mixed phases of anatase and rutile, eventually, the single nanotubes would collapse⁴⁰. Therefore, only pure amorphous and anatase nanotubes were investigated.

Bundles of nanotubes were scratched off the foil onto commercial, p-boron doped silicon substrates ($5 \times 5 \text{ mm}$) with a 150 nm SiN_x coating, see FIG. 1(b). By applying pressure and a slow circular motion using a second substrate, some single nanotubes break off the bundles and were stuck to the substrates because of electrostatic attraction. Suitable tubes were selected using an optical microscope. In order to fix the nanotubes on the substrate and to prepare them for contacting, electron beam induced deposition (EBID) of tungsten carbide was used, see FIG. 1(c). The deposited WC_x is nearly insulating⁴² and provides the necessary steps to compensate the height difference between contacts and nanotube. The substrates were covered with a positive working resist (ALL-RESIST, PMMA 950 K, AP-R 671-05) and, by means of electron beam lithography (EBL), the structures of the contacts were printed into the resist. After developing, a bilayer film composed of Cr (5 nm) and Au (35 nm) was sputtered. The PMMA was later removed by acetone. The width of the contacts exceeds the WC_x steps, in order to get a potential barrier-free electrical connection. A prepared nanotube can be seen in FIG. 1(d). An overview of the structural properties and dimensions of the nanotubes can be seen in Table I.

For the transport measurements, each sample was contacted on a chip carrier placed on the cold head of a standard closed cycle cooling system inside a vacuum bell with a minimum temperature of $T \approx 30 \text{ K}$. The electrical resistance was measured using the four-point probe configuration with a current source (Keithley 6221) and a nano-voltmeter (Keithley 2182). The high resistance measurements were performed with a constant applied voltage using a DC source (Yokogawa 7651). The current was monitored with a shunt resistance of $R_s = 9.101 \text{ M}\Omega$ in series with the samples. For low temperature measurements down to $T = 5 \text{ K}$, a commercial ^4He cryostat (Oxford Instruments) was used.

The Ar ion irradiation was done in a self-made plasma chamber with a parallel plate (copper) setup at room temperature. The chamber was evacuated to a pressure of $P \approx 0.1 \text{ mbar}$ with an Ar/H gas mixture (Ar: 90 % and H: 10 %, Air Liquide) flowing through the chamber. The chip carriers with samples were mounted $\approx 12 \text{ cm}$ away

from the plasma center and a bias voltage of $U_{\text{bias}} = 50$ V was used to accelerate the ions towards the sample, while connected to ground, and the bias current was measured. The energy used is too low to produce any relevant sputtering, which could induce a composition variation. Previously, the substrate was covered with PMMA and a window was opened to shield the contacts using electron beam lithography. The number of ions hitting the sample was estimated to be $\approx 2.2 \times 10^{14}$ Ar ions²³.

Information about the sample structure was obtained using the confocal Raman microscope alpha300R+ from WITec with an incident laser light of wavelength $\lambda = 532$ nm. The device has a lateral resolution of ≈ 300 nm and a depth resolution of ≈ 900 nm. The energy was kept at ≈ 3 mW to avoid damage caused by heating effects in the sample.

III. RESULTS

Using XRD, it was shown that the as-prepared nanotube bundles are amorphous and they transform into anatase after annealing^{39,40}. However, some single nanotubes could remain in the amorphous state. Using confocal Raman spectroscopy, single isolated samples can be investigated. According to Ohsaka *et al.*⁴³ for bulk anatase, Raman peaks can be found at 639 cm^{-1} , 197 cm^{-1} and 144 cm^{-1} , assigned as E_g modes. B_{1g} modes are at 513 cm^{-1} and 399 cm^{-1} , and the band at 519 cm^{-1} corresponds to the A_{1g} mode. The Raman E_g band at 144 cm^{-1} is the most intense peak. Our results are presented in FIG. 1(e), the peaks correspond to the E_g band, the obtained values are 148 cm^{-1} and 633 cm^{-1} , respectively, which are different compared to the above mentioned results for the bulk anatase. This band shift is known as blueshift and is caused due to phonon confinement in the nanocrystals forming the nanotube. This effect was already reported for anatase nanocrystals⁴⁴, where the shift of the E_g peak as a function of the annealing temperature was investigated. A blueshift to 148 cm^{-1} was obtained for nanocrystals annealed at $\approx 350^\circ$ C, which is in agreement with the annealing temperature used for the TiO_2 nanotube. From the blueshift, a crystallite size of ≈ 8 nm could be obtained⁴⁴, which is in agreement with XRD results⁴⁰. A $(x - y)$ Raman scan is shown in the inset of FIG. 1(e), where the bright shades correspond to the Raman E_g band at 148 cm^{-1} .

The electrical properties of the nanotubes depend strongly upon the phase and structural quality. A defect free TiO_2 anatase nanotubes is electrical insulating. However, due to growth conditions, defects can be introduced resulting in an electrical conductive material. For example, such defects are oxygen vacancies (self doping) produced by a reduction of TiO_2 , e.g. through electrochemical reactions, gas annealing or exposure to vacuum^{40,45–47}, due to a separation of O_2 or H_2O from terminal oxide or hydroxide groups and bridged oxide and Ti^{3+}

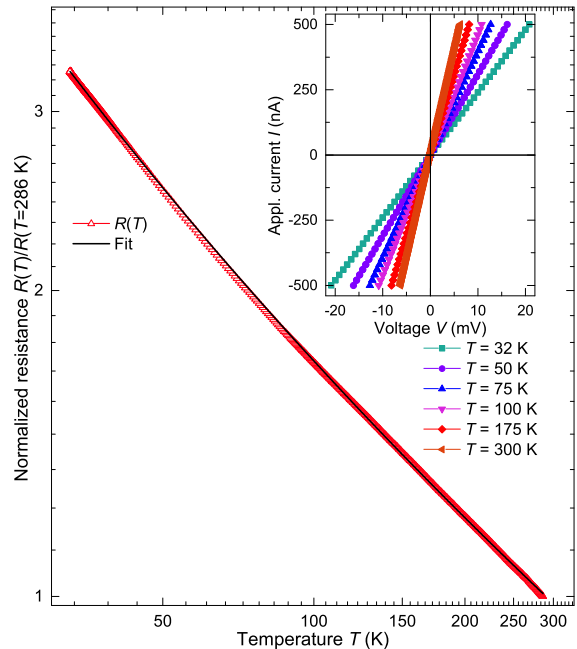


FIG. 2. The temperature dependent resistance of nanotube NT1 is shown. In the inset the linear $I - V$ curves can be seen. The continuous line was obtained from Eq. (1).

states⁴⁶. Many investigated nanowires and/or nanotubes exhibit non-linear $I - V$ curves, which are usually neither discussed, nor explained in the literature⁴⁸. Such non-ohmic behavior could be due to intergrain conduction or barriers formed on the contacts used for measurements. For convenience, the measured samples in this work are sorted in three categories: polycrystalline nanotubes with linear (Section III A) and non-linear (Section III B) $I - V$ curves, an amorphous sample (Section III C) and an insulating anatase nanotube which was treated with low-energy Ar ions (Section III D).

A. Linear $I - V$ curves

The TiO_2 nanotube sample NT1 shows linear $I - V$ curves in the whole investigated temperature range, see inset in FIG. 2. Similar results were already shown in previous work³⁰. The measurements were carried out using the four-point probes method. The temperature dependence of the resistance can be seen in FIG. 2, which can be fitted using the Mott variable range hopping (VRH) model³⁰:

$$R_{\text{VRH}}^{-1}(T) = \left\{ R_2 \exp \left[\left(\frac{T_h}{T} \right)^{1/(1+d)} \right] \right\}^{-1} + R_0^{-1}, \quad (1)$$

where R_2 is an arbitrary prefactor, R_0 is a temperature independent term, the dimensionality $d = 3$

and T_h is a characteristic temperature. From the fit, $T_h = (3450 \pm 29)$ K; similar values have already been reported in the literature³⁰. The density of states (DOS) at the Fermi level $N(E_F)$ can then be calculated:

$$T_h = \frac{18}{k_B \xi^3 N(E_F)}, \quad (2)$$

where k_B is Boltzmann constant and the localization length is assumed to be in the order of $\xi = 1$ nm⁴⁹. A DOS of $N(E_F) \approx 6.1 \times 10^{28} \text{ eV}^{-1} \text{ m}^{-3}$ was found, which agrees very well with the literature^{30,50}. The resistivity, see Table I, is very low compared to other investigated samples. The low resistivity might be a consequence of doping due to a large density of defects present in the sample.

B. Non-linear $I - V$ curves

The current-voltage characteristics using Mott VRH and activated transport processes correspond to linear $I - V$ curves (ohmic regime). Therefore, they fail to explain non-linear $I - V$ curves as well as $R(T)$ for such samples. The conduction of the polycrystalline nanotube depends on the intragrain and intergrain conductivity. When there is no doping, the grains are insulating with an energy gap of ≈ 3 eV. At intermediate doping, the charge carriers move to the crystal defects/boundaries between the grains, which are acting as electronic traps, and thus a depletion layer is formed with a potential barrier. In this case non-linear $I - V$ curves can be observed also when measuring with four-point probes method. At high doping levels, the material is saturated and the barrier vanishes again.

The nanotube NT2 was measured using four contacts and shows non-linear $I - V$ curves, see inset FIG. 3. The $I - V$ measurements were performed from $T = 50$ K to $T = 300$ K, where non-linear behavior can be observed at temperatures $T \leq 175$ K and below. This can also be seen in the temperature dependent resistance measurements, which were done using $I = 100$ nA and $I = 200$ nA, at $T \leq 175$ K the curves split. The non-linearity of the $I - V$ curves and the temperature dependence can be explained using the fluctuation induced tunneling conductance (FITC) model, which was already used to describe similar materials such as nanoporous TiO₂ thin films³⁶, ZnO nanowires²⁷, oxide nanostructures^{51–53}, double walled carbon nanotube bundles³⁵ or disordered semiconductors⁵⁴. According to the FITC model, at small applied electric fields, the temperature dependent resistance across a junction is given by³⁴

$$R_{\text{FITC}}^{-1} = \left(R_\infty \exp \left[\frac{T_1}{T_0 + T} \right] \right)^{-1} + R_0^{-1}, \quad (3)$$

where R_∞ is a free, temperature independent parameter,

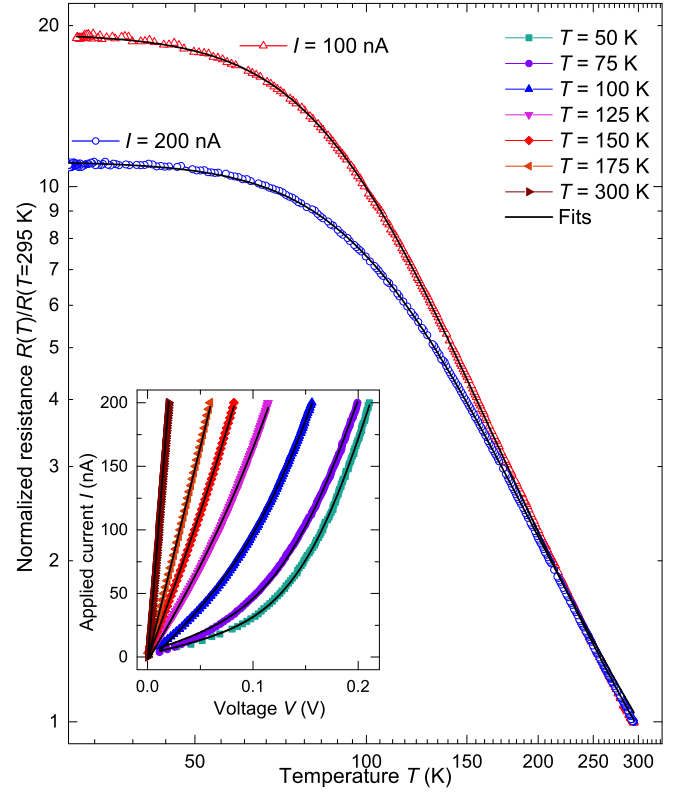


FIG. 3. The temperature dependent measurements at two applied currents of sample NT2 are presented. The resistance at room temperature is $R_{\text{RT}} = 100$ k Ω . The inset shows the $I - V$ curves at different temperatures. The continuous lines are the fits obtained following Eq. (3) for $R(T)$ and Eq. (5) for the $I - V$ curves.

and the characteristic temperatures are defined as

$$\begin{aligned} T_1 &= \frac{8\epsilon_r\epsilon_0 A\varphi_0^2}{e^2 k_B w}, \\ T_0 &= \frac{16\epsilon_r\epsilon_0 \hbar A\varphi_0^{3/2}}{\pi\sqrt{2mk_B} e^2 w^2}, \end{aligned} \quad (4)$$

where ϵ_0 is the vacuum permittivity, ϵ_r the dielectric constant of the barrier, e the elementary charge, k_B is the Boltzmann constant, \hbar the reduced Planck constant, m the electron mass, A the area of the tunnel junction, φ_0 the barrier height and w is the barrier width. The characteristic energy T_1 can be regarded as the energy required for an electron to pass the barrier and T_0 is the temperature for which well below thermal fluctuations become insignificant. As stated before, the FITC model also provides the means to describe the non-linear $I - V$ curves at different temperatures as follows³⁴:

$$I_{\text{FITC}} = I_s \exp \left[-a(T) \left(1 - \frac{V}{V_c} \right)^2 \right], |V| < V_c, \quad (5)$$

where I_s and V_c are the saturation current and critical

voltage, respectively, and $a(T)$ is given as:

$$a(T) = \frac{T_1}{T_0 + T}. \quad (6)$$

As can be seen from these equations, the characteristic temperatures can be obtained through fitting the $I - V$ curves and the temperature dependent resistance $R(T)$. However, in order to fit the data, a temperature independent term R_0 in parallel to the FITC conduction process, has to be added. The parallel contribution is due to disorder and impurities present in the TiO₂ nanotubes.

In order to fit the data and to reduce the amount of free parameters, all curves were fitted simultaneously ($I - V$ curves and $R(T)$) and the corresponding parameters were taken as shared parameters for all curves. This means, that V_c and I_s (which depend only weakly on the temperature) are shared among the data of the $I - V$ curves, and that T_1 and T_0 are shared among the $I - V$ curves and $R(T)$ results. The data and the fits can be seen in FIG. 3, the FITC model describes very well both the $I - V$ curves and $R(T)$ results. From the fit results, a saturation current of $I_s \approx 2.8 \times 10^{-7}$ A and a critical voltage of $V_c \approx 0.29$ V are obtained. The characteristic temperatures are $T_1 \approx 853$ K and $T_0 \approx 59$ K. Similar values have already been reported in the literature^{27,52,53,55}. Although, the samples were measured using the four-point probes method, non-linear $I - V$ curves were measured as consequence of barriers formed at the intergrain boundaries. This effect could be avoided by employing long term annealing at intermediate temperatures, as high-temperature annealing would result in a collapse of the TiO₂ nanotubes^{40,41,56,57}.

C. Amorphous nanotube

The temperature dependent resistance of an amorphous TiO₂ nanotube NT3 is shown in FIG. 4. The room temperature resistance is $R(295 \text{ K}) = 29 \text{ M}\Omega$, and thus much higher than the previously shown samples. Therefore, the resistance was measured with a constant applied voltage of $V = 10 \text{ V}$ and the current was monitored with a shunt resistance. This implies a two point-probes technique to be used. However, a large influence of the contacts is not expected, due to the very high resistance of the TiO₂ nanotube itself. This assumption is supported by the result of a four-point probes measurement at room temperature, which yields the same resistance as for the two-point measurement. Therefore, the influence of the contacts will be neglected. The data as well as the fits are shown in FIG. 4, in the inset the $I - V$ curves can be seen. As before, all measurements were fitted simultaneously. In order to fit the $R(T)$ data, not only the FITC model has to be assumed but also a VRH hopping contribution in parallel was needed, see Eq. (1). The shared parameters were: $I_s = 5.5 \pm 0.1 \times 10^{-5}$ A, $V_c = 144 \pm 3$ V, $T_1 = 6545 \pm 50$ and $T_0 = 272 \pm 7$ K. With the characteristic temperature $T_h \approx 70000$ K and using Eq. (2), the

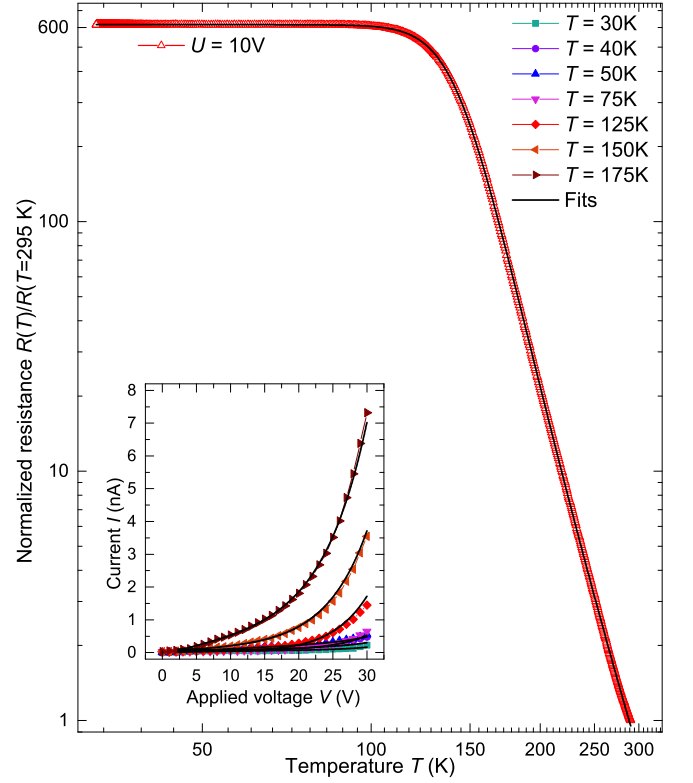


FIG. 4. The temperature dependent measurements at constant applied voltage of sample NT3 are presented. The resistance at room temperature is $R_{RT} = 29 \text{ M}\Omega$. The inset shows the $I - V$ curves at different temperatures. The continuous lines are the fits obtained following Eq. (1) and Eq. (3) for $R(T)$, and Eq. (5) for the $I - V$ curves.

DOS at E_F is $N(E_F) \approx 3 \times 10^{27} \text{ eV}^{-1} \text{ m}^{-3}$. This value is one order of magnitude smaller than what was obtained for TiO₂ nanotube with linear $I - V$ curves. This together with the large values of T_1 and T_0 , i.e. large barrier height, explain the high resistance of this sample. At low temperature, the constant R_0 term in parallel which is due to impurities/defects, dominates the transport.

D. Ar ion irradiated nanotube

In order to investigate the influence of defects on the transport properties of polycrystalline anatase TiO₂ nanotubes, an almost insulating sample was chosen (see results in FIG. 5), indicating a high quality of the crystalline structure. The sample NT4 has been irradiated using an Ar/H plasma. The results after irradiation of the temperature dependent resistance measurements and $I - V$ curves can be seen in FIG. 5 and its inset. The used energy of the plasma ions of 50 V and, according to SRIM simulations, the resulting penetration depth is $\approx 5 \text{ nm}$, implying that the nanotube is modified only at the surface^{23,27}. The sample consists then of an insulating polycrystalline nanotube surrounded by a conduct-

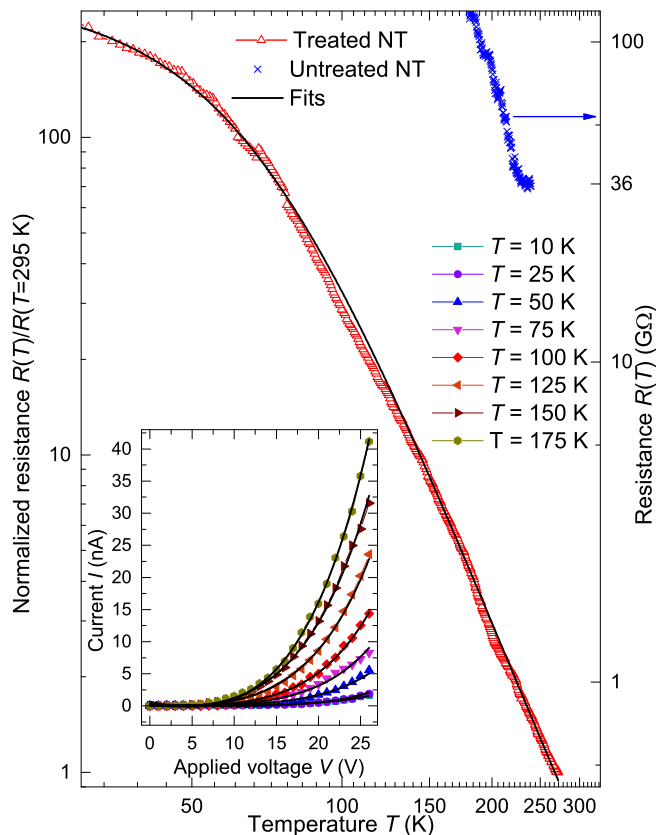


FIG. 5. The results of the temperature dependent measurements at constant applied voltage of sample NT4 after Ar/H ion irradiation are presented. The resistance at RT is $R_{RT} = 500 \text{ M}\Omega$. The inset shows the $I - V$ curves at different temperatures. The continuous lines are the fits obtained following Eq. (3) for $R(T)$ and Eq. (5) for the $I - V$ curves. The resistance before ion irradiation was $R_i = 36 \text{ G}\Omega$ at $T = 240 \text{ K}$ and is indicated with blue crosses.

ing TiO_2 shell. The FITC model is suitable to describe such systems, which is in agreement with the non-linear $I - V$ curves. Although the sample was irradiated homogeneously, the conduction can be well described by the FITC model. This indicates that the defects produced in the grains induce finite conductivity, yet the regions between the grains, i.e. the grain boundaries, remain insulating and are less affected by defects. The sample was measured using the two-point probes method and shunt resistance. Due to the high intrinsic resistance, the contact contribution is neglected. The $I - V$ curves and $R(T)$ were fitted as before, using the characteristic temperatures T_1 and T_0 and the saturation current I_s and critical voltage V_c as shared parameters. The model to fit the data was the same as for the other polycrystalline sample with non-linear $I - V$ curves, i.e. the FITC model in par-

allel with a temperature independent residual resistance. The obtained parameters are $I_s = 7.9 \pm 0.6 \times 10^{-6} \text{ A}$, $V_c = 116 \pm 10 \text{ V}$, $T_1 = 3106 \pm 80$ and $T_0 = 206 \pm 4 \text{ K}$. This indicates a larger barrier height compared to the other polycrystalline samples. The estimated resistivity, see Table I, is larger than of sample NT2, indicating a relative low defect production probability with the used energy.

IV. CONCLUSION

Several anodically grown amorphous and polycrystalline TiO_2 nanotubes were isolated and prepared for the measurement of their electrical transport properties. Raman spectroscopy reveals that the investigated anatase samples are homogeneous and polycrystalline with a grain size of a few nanometers. For nanotubes with linear $I - V$ characteristics a VRH transport mechanism explains the measured behavior. In order to describe the $R(T)$ and non-linear $I - V$ curves, the FITC as well as the VRH model are used. Using four contacts, non-linear $I - V$ curves were measured, which can be explained considering a barrier formed at the interfaces between the grains. The fluctuation induced tunneling conductance describes the resistance results as well as the non-linear $I - V$ curves for the polycrystalline TiO_2 nanotubes. A combination of the FITC model and VRH was used for the analysis of the resistance of an amorphous nanotube. The contacts on the crystalline samples are ohmic, i.e. there is no barrier, which is important for future studies and applications. An insulating sample was irradiated with low-energy Ar/H plasma, and a large change in the resistivity was produced. This provides the possibility to modify the electrical transport properties of individual TiO_2 nanotubes through controlled irradiation with ions. In this work, the preparation of single TiO_2 nanotubes with ohmic contacts for electrical transport measurements was demonstrated, which opens new possibilities for future applications.

ACKNOWLEDGMENTS

This work was supported by DFG through the Collaborative Research Center SFB 762 “Functionality of Oxide Interfaces”.

BIBLIOGRAPHY

* markus@mstiller.org

¹ K. I. Hadjiivanov and D. G. Klissurski, Chem. Soc. Rev **25**, 61 (1996).

- ² A. Fujishima and K. Honda, *Nature* **238**, 37 (1972).
- ³ B. O'Regan and M. Grätzel, *Nature* **353**, 737 (1991).
- ⁴ M.-H. Seo, M. Yuasa, T. Kida, J.-S. Huh, K. Shimano, and N. Yamazoe, *Sen. and Act. B: Chemical* **137**, 512 (2009).
- ⁵ M. M. Momeni and Y. Ghayeb, *J. of Alloys and Compounds* **637**, 393 (2015).
- ⁶ M. M. Momeni and Y. Ghayeb, *J. of Appl. Electrochem.* **45**, 557 (2015).
- ⁷ A. S. Aricó, P. Bruce, B. Scrosati, J.-M. Tarascon, and W. van Schalkwijk, *Nature* **4**, 366 (2005).
- ⁸ T. W. Woolerton, S. Sheard, E. Reisner, E. Pierce, S. W. Ragsdale, and F. A. Armstrong, *J. of Am. Chem. Soc.* **132**, 2132 (2010).
- ⁹ O. K. Varghese, M. Paulose, T. J. LaTempa, and C. A. Grimes, *Nano Lett.* **9**, 731 (2009).
- ¹⁰ D. Zhao, C. Chen, K. Yao, X. Shi, Z. Wang, H. Hahn, H. Gleiter, and N. Chen, *J. of All. and Comp.* (2016), 10.1016/j.jallcom.2016.09.183.
- ¹¹ U. Diebold, *Surf. Sci. Rep.* **48**, 53 (2003).
- ¹² X. Chen and S. S. Mao, *Chem. Rev.* **107**, 2891 (2007).
- ¹³ H. Tang, K. Prasad, R. Sanjines, P. Schmid, and F. Lévy, *J. Appl. Phys.* **75**, 2042 (1994).
- ¹⁴ M. Momeni, Y. Ghayeb, and S. Gheibee, *Ceramics International* **43**, 564 (2017).
- ¹⁵ M. M. Momeni and Y. Ghayeb, *Ceramics International* **42**, 7014 (2016).
- ¹⁶ M. M. Momeni, Y. Ghayeb, and M. Davarzadeh, *J. of Electroanalytical Chemistry* **739**, 149 (2015).
- ¹⁷ M. M. Momeni and Y. Ghayeb, *J. of Mol. Catal. A: Chemical* **417**, 107 (2016).
- ¹⁸ M. M. Momeni, Y. Ghayeb, and Z. Ghonchehi, *Ceramics International* **41**, 8735 (2015).
- ¹⁹ M. Momeni and I. Ahadzadeh, *Mat. Res. Innov.* **20**, 44 (2016).
- ²⁰ G. K. Mor, O. K. Varghese, M. Paulose, K. Shankar, and C. A. Grimes, *Sol. En. Mat. and Sol. Cel.* **90**, 2011 (2006).
- ²¹ Y. Lai, L. Sun, C. Chen, C. Nie, J. Zuo, and C. Lin, *Appl. Surf. Sci.* **252**, 1101 (2005).
- ²² B. Choudhury and A. Choudhury, *J. Appl. Physics* **114**, 203906 (2013).
- ²³ M. Stiller, J. Barzola-Quiquia, P. Esquinazi, D. Spemann, J. Meijer, M. Lorenz, and M. Grundmann, *AIP Advances* **6**, 125009 (2016).
- ²⁴ R. Sanjines, H. Tang, H. Berger, F. Gozzo, G. Margaritondo, and F. Levy, *J. of Appl. Phys.* **75**, 2945 (1994).
- ²⁵ J. Pascual, J. Camassel, and H. Mathieu, *Phys. Rev. B* **18**, 5606 (1978).
- ²⁶ A. Muñoz, *Electrochimica Acta* **52**, 4167 (2007).
- ²⁷ M. Stiller, J. Barzola-Quiquia, M. Zoraghi, and P. Esquinazi, *Nanotechnology* **26**, 395703 (2015).
- ²⁸ K. D. Sattler, ed., *Handbook of Nanophysics: Nanotubes and Nanowires* (CRC Press, New York, USA, 2011).
- ²⁹ A. Tighineanu, T. Ruff, S. Albu, R. Hahn, and P. Schmuki, *Chem. Phys. Lett.* **494**, 260 (2010).
- ³⁰ M. Stiller, J. Barzola-Quiquia, I. Lorite, P. Esquinazi, R. Kirchgeorg, S. P. Albu, and P. Schmuki, *Appl. Phys. Lett.* **103**, 173108 (2013).
- ³¹ C. Fàbrega, F. Hernández-Ramírez, J. D. Prades, R. Jiménez-Díaz, T. Andreu, and J. R. Morante, *Nanotechnology* **21**, 445703 (2010).
- ³² A. Akl, H. Kamal, and K.A.-Hady, *Appl. Surf. Sci.* **252**, 8651 (2006).
- ³³ B. Huber, H. Gnaser, and C. Ziegler, *Surf. Sci.* **566-568**, 419 (2004).
- ³⁴ P. Sheng, *Phys. Rev. B* **21**, 2180 (1980).
- ³⁵ J. Barzola-Quiquia, P. Esquinazi, M. Lindel, D. Spemann, M. Muallem, and G. Nessim, *Carbon* **88**, 16 (2015).
- ³⁶ S. J. Konezny, C. Richter, R. C. Snoeberger, A. R. Parent, G. W. Brudvig, C. A. Schmuttenmaer, and V. S. Batista, *Phys. Chem. Lett.* **2**, 1931 (2011).
- ³⁷ A. Hassan, N. Chaure, A. Ray, A. Nabok, and S. Habesch, *J. Phys. D: Appl. Phys.* **36**, 1120 (2003).
- ³⁸ E. Barborinia, G. Bongiorno, A. Forleob, L. Franciosob, P. Milania, I. Kholmanovc, P. Piseria, P. Sicilianob, A. Taurinob, and S. Vinatia, *Sensors and Actuators B: Chemical* **111-112**, 22 (2005).
- ³⁹ S. P. Albu, H. Tsuchiya, S. Fujimoto, and P. Schmuki, *Eur. J. Inorg. Chem.* **2010**, 4351 (2010).
- ⁴⁰ K. Lee, A. Mazare, and P. Schmuki, *Chemical Reviews* **114**, 9385 (2014).
- ⁴¹ S. Soa, I. Hwanga, F. Ribonia, J. Yooa, and P. Schmuki, *Electrochem. Comm.* **71**, 73 (2016).
- ⁴² D. Spoddig, K. Schindler, P. Rödiger, J. Barzola-Quiquia, K. Fritsch, H. Mulders, and P. Esquinazi, *Nanotechnology* **18**, 495202 (2007).
- ⁴³ T. Ohsaka, F. Izumi, and Y. Fujiki, *J. of Raman Spec.* **7**, 321 (1978).
- ⁴⁴ W. Zhang, Y. He, M. Zhang, Z. Yin, and Q. Chen, *J. of Phys. D: Appl. Phys.* **33**, 912 (2000).
- ⁴⁵ N. Liu, C. Schneider, D. Freitag, M. Hartmann, U. Venkatesan, J. Mller, E. Spiecker, and P. Schmuki, *Nano Lett.* **14**, 3309 (2014).
- ⁴⁶ I. Paramasivam, H. Jha, N. Liu, and P. Schmuki, *small* **8**, 3073 (2012).
- ⁴⁷ A. Ghicov, H. Tsuchiya, J. M. Macak, and P. Schmuki, *phys. stat. sol. a* **203**, R28 (2006).
- ⁴⁸ S.-P. Chiu, Y.-H. Lin, and J.-J. Lin, *Nanotechnology* **20**, 015203 (2009).
- ⁴⁹ L. X. Chen, T. Rajh, Z. Wang, and M. C. Thurnauer, *J. Phys. Chem B* **101**, 10688 (1997).
- ⁵⁰ A. Yildiz, S. B. Lisesivdin, M. Kasap, and D. Mardare, *Optoelectronics and Advanced Materials - Rapid Communications* **1**, 5 (2008).
- ⁵¹ C. Filipi, A. Levstik, Z. Kutnjak, P. Umek, and D. Aron, *J. Appl. Phys.* **101**, 084308 (2007).
- ⁵² Y.-H. Lin, S.-P. Chiu, and J.-J. Lin, *Nanotechnology* **19**, 365201 (2008).
- ⁵³ Y.-H. Lin and J.-J. Lin, *J. of Appl. Phys.* **110**, 064318 (2011).
- ⁵⁴ D. Redfield, *Advances in Phys.* **24**, 463 (1975).
- ⁵⁵ H. Xie and P. Sheng, *Phys. Rev. B* **79**, 165419 (2009).
- ⁵⁶ S. P. Albu, A. Ghicov, S. Aldabergenova, P. Drechsel, D. LeClere, G. E. Thompson, J. M. Macak, and P. Schmuki, *Adv. Mat.* **20**, 4135 (2008).
- ⁵⁷ F. Mohammadpour, M. Altomare, S. So, K. Lee, and M. Mokhtar, *Semicond. Sci. and Techn.* **31**, 014010 (2016).